Atmos. Meas. Tech., 3, 1599–1613, 2010
www.atmos-meas-tech.net/3/1599/2010/
doi:10.5194/amt-3-1599-2010

Atmospheric Measurement Techniques

H_2O and δD profiles remotely-sensed from ground in different spectral infrared regions

M. Schneider[1,*], G. C. Toon[2], J.-F. Blavier[2], F. Hase[1], and T. Leblanc[3]

[1]Karlsruhe Institute of Technology (KIT), IMK-ASF, Karlsruhe, Germany
[2]Jet Propulsion Laboratory (JPL), California Institute of Technology, Pasadena, USA
[3]Jet Propulsion Laboratory (JPL), California Institute of Technology, Wrightwood, USA
[*]now at: Agencia Estatal de Meteorología (AEMET), CIAI, Santa Cruz de Tenerife, Spain

Received: 14 July 2010 – Published in Atmos. Meas. Tech. Discuss.: 23 July 2010
Revised: 14 November 2010 – Accepted: 15 November 2010 – Published: 22 November 2010

Abstract. We present ground-based FTIR (Fourier Transform Infrared) water vapour analyses performed in four different spectral regions: 790–880, 1090–1330, 2650–3180, and 4560–4710 cm^{-1}. All four regions allow the retrieval of lower, middle, and upper tropospheric water vapour amounts with a vertical resolution of about 3, 6, and 10 km, respectively. In addition the analyses at 1090–1330 and 2650–3180 cm^{-1} allow the retrieval of lower and middle/upper tropospheric δD values with vertical resolutions of 3 and 10 km, respectively. A theoretical and empirical error assessment – taking coincident Vaisala RS92 radiosonde measurements as a reference – suggests that the H_2O data retrieved at high wavenumbers are slightly more precise than those retrieved at low wavenumbers. We deduce an H_2O profile precision and accuracy of generally better than 20% except for the low wavenumber retrieval at 790–880 cm^{-1}, where the assessed upper precision limit of middle/upper tropospheric H_2O is 35%. The scatter between the H_2O profiles produced by the four different retrievals is generally below 20% and the bias below 10%, except for the boundary layer, where it can reach 24%. These values well confirm the theoretical and empirical error assessment and are rather small compared to the huge tropospheric H_2O variability of about one order of magnitude thereby demonstrating the large consistency between the different H_2O profile retrievals. By comparing the two δD profile versions we deduce a precision of about 8 and 17‰ for the lower and middle/upper troposphere, respectively. However, at the same time we observe a systematic difference between the two retrievals of up to 40‰ in the middle/upper troposphere which is a large value compared to the typical tropospheric δD variability of only 80‰.

Correspondence to: M. Schneider
(matthias.schneider@kit.edu)

1 Introduction

The Fourth Assessment Report of the Intergovernmental Panel on Climate Change describes the insufficient understanding of the atmospheric water cycle as a major source of uncertainties of climate projections (Randall et al., 2007). Understanding the atmospheric water sources (evaporation from ocean or land), sinks (precipitation), and transport (advection, diffusion, turbulence, inner-cloud processes, etc.) is essential for understanding and predicting climate change. It requires continuous, high quality, and consistent long-term observations on a global scale.

In the framework of the NDACC (Network for the Detection of Atmospheric Composition Change, Kurylo and Zander, 2000) about 20 ground-based FTIR spectrometers have measured high quality solar absorption spectra in the mid-infrared over many years and at many different globally distributed sites. Currently the TCCON (Total Carbon Column Observing Network, Wunch et al., 2010) is establishing and measures high quality solar absorption spectra in the near infrared at about 15 globally distributed sites with almost the same type of FTIR instrument. High quality ground-based FTIR networks can provide consistent long-term water vapour data with some global representativeness. In order to achieve an optimal signal to noise ratio most ground-based FTIR instruments use optical filters and measure the different spectral infrared regions by a sequence

Published by Copernicus Publications on behalf of the European Geosciences Union.

of measurements. There are several publication that report ground-based FTIR water vapour retrievals in different spectral regions: 1110–1122 cm^{-1} (Schneider et al., 2006a); 1110–1122 and 1220–1330 cm^{-1} (Schneider et al., 2006b); 790–880 and 1090–1330 cm^{-1} (Schneider and Hase, 2009b; Schneider et al., 2010a); 840–860 cm^{-1} (Sussmann et al., 2009); 3260–3310 cm^{-1} (Palm et al., 2010).

Simultaneous observation of the different tropospheric water vapour isotopologues are particularly useful for water cycle research. The isotopologue ratios are sensitive to the original moisture source (e.g., Craig, 1961) and can be used for investigating different hydrological processes in the troposphere (e.g., Worden et al., 2007; Yoshimura et al., 2008; Risi et al., 2008; Frankenberg et al., 2009). However, it is extremely difficult to measure tropospheric water vapour isotopologue ratios to a worthwhile accuracy. Nevertheless, it has been demonstrated by Schneider et al. (2010b) that the NDACC FTIR's can provide consistent long-term observations of simultaneous tropospheric H_2O and δD profiles with a sufficiently high precision. Here and in the following the ratio between $HD^{16}O$ and $H_2^{16}O$ is expressed in the δ-notation: $\delta D = 1000 \times (\frac{[HD^{16}O]/[H_2^{16}O]}{SMOW} - 1)$, whereby $SMOW = 3.1152 \times 10^{-4}$ (with SMOW: Standard Mean Ocean Water).

Area-wide coverage can only be achieved by space-based measurements. Currently there are several sensors in space with the capability to observe tropospheric H_2O and δD simultaneously: ACE (Atmospheric Chemistry Experiment, Nassar et al., 2007), TES (Tropospheric Emission Spectrometer, Worden et al., 2006), SCIAMACHY (Scanning Imaging Absorption Spectrometer for Atmospheric Chartography, Frankenberg et al., 2009), GOSAT (Greenhouse Gases Observing Satellite, Kuze et al., 2009), and IASI (Infrared Atmospheric Sounding Interferometer, Herbin et al., 2009). The different space-based sensors have different sensitivities: ACE, TES, and IASI measure mainly upper and middle tropospheric H_2O and δD whereas SCIAMACHY and GOSAT can detect column integrated H_2O and δD. A comprehensive satellite sensor validation requires tropospheric H_2O and δD profiles as reference, and the ground-based FTIR technique is unique in providing such data on a continuous basis.

In this paper we assess the quality and consistency of tropospheric H_2O and δD profiles remotely-sensed by ground-based FTIR in four different spectral regions: 790–880, 1090–1330, 2650–3180, and 4560–4710 cm^{-1}. Such assessment is important when applying the FTIR H_2O and δD data for research purposes and for satellite validation. We perform theoretical and empirical error assessments. Furthermore, we document the level of consistency between the different H_2O and δD retrievals. We analyse 325 spectra measured by the Jet Propulsion Laboratory's (JPL) MkIV FTIR spectrometer during the MOHAVE-2009 campaign (MOHAVE: Measurements of Humidity in the Atmosphere and Validation Experiments), which took place in October 2009 at JPL Table Mountain Facility, California, USA. The MkIV covers a very broad infrared range (650–5650 cm^{-1}) in a single measurement, which assures us that the absorption signatures recorded in the different spectral regions are produced by the same airmass and that our consistency study is not influenced by atmospheric variability. Such consistency study gives additional information about the precision and accuracy of the ground-based FTIR H_2O and δD products and documents the feasibility of interchangeably using H_2O and δD profiles retrieved from different spectral regions.

In Sect. 2 we give a brief description of the MOHAVE-2009 campaign and the MkIV spectrometer. Section 3 presents the analysed spectral regions. Section 4 documents the theoretical performance of the retrievals and extensively estimates the errors of the remotely-sensed products for each of the different retrievals. Section 5 and 6 compare the retrievals to coincident radiosonde measurements and document their consistency. Our study is summarised in Sect. 7.

2 FTIR measurements during MOHAVE-2009

The MOHAVE-2009 campaign took place at the JPL Table Mountain Facility (TMF) in October 2009: http://tmf-lidar.jpl.nasa.gov/campaigns/mohave2009.htm. For the campaign a large variety of different experiments performed side-by-side water vapour measurements from the ground to the mesopause:

- 3 water vapour Raman lidars: nighttime measurements, vertical range: ground-20 km.
- 15 cyrogenic frostpoint hygrometers and 3 frost-point hygrometer radiosondes: during night (in coincidence with lidar observations), vertical range: ground-30 km.
- 50 Vaisala RS92 radiosondes: Mostly during night, vertical range: ground-15 km.
- 2 microwave radiometers: night and day, vertical range: 20–80 km.
- 2 GPS (Global Positioning System) receivers: night and day, only total column amounts.
- FTUVS (Fourier Transform Ultraviolet Spectrometer): daytime measurements, only total column amounts.
- The MkIV FTIR: daytime measurements, vertical range: from the ground to the upper tropopause.

In addition, measurements were performed in coordination with satellite overpasses (Aura MLS, Aura TES, Aqua AIRS, ACE, and MIPAS). The main focus of the campaign was a further development and a quality assessment of the water vapour lidar technique. Therefore, most measurements were performed during night.

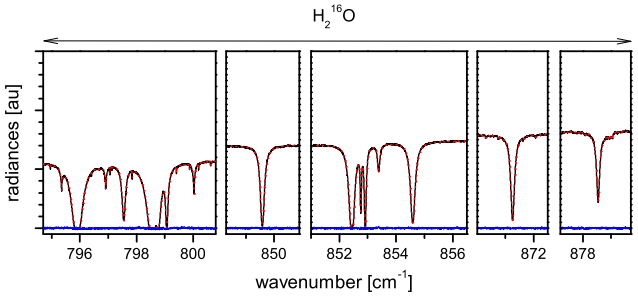

Fig. 1. Spectral microwindows of the 790–880 cm^{-1} retrieval taken from a spectra measured on the 18th of October 2009, at a solar elevation of 17.8°, and for a total water vapour column amount of 5 mm. Black line: measured spectrum; Red line: simulated spectrum; Blue line: residuals (difference between measurement and simulation).

The MkIV FTIR spectrometer was designed and built at the Jet Propulsion Laboratory in 1984. Since then it has been operated on different platforms (ground-, balloon-, and aircraft-based) in the framework of a large variety of different campaigns mainly dedicated to the investigation of stratospheric ozone chemistry. The MkIV can measure high resolution spectra (maximal optical path difference of 200 cm) and covers a very broad spectral range (650–5650 cm^{-1}), whereby two liquid nitrogen-cooled detectors are applied: an HgCdTe photoconductor (for wavenumbers below 1850 cm^{-1}) and an InSb photodiode for higher wavenumbers. The two detector design prevents photon noise from the high frequencies, where the sun is brighter, from degrading the signals at the lower frequencies. Simultaneous high-resolution measurement over such a wide spectral region imposes severe constraints on the dynamic range and linearity required of the detectors, pre-amplifiers, and signal chains. In the MkIV, this problem is addressed by using of an 18-bit ADC module. More details about the MkIV spectrometer can be found in Toon (1991) and on the web page: http://mark4sun.jpl.nasa.gov/.

3 The analysis in different spectral regions

We analyse the spectra with the algorithm PROFFIT (Hase et al., 2004), which consists of a precise line-by-line radiative transfer model and an inversion algorithm based on the optimal estimation approach (Rodgers, 2000). We deduce the required H_2O a priori information – the climatologic mean profile and its covariance – from Vaisala RS92 radiosonde measurements performed on the subtropical island of Tenerife between 2005 and 2009 (the radiosondes are launched twice daily). As δD a priori profile information we use the mean and covariance calculated from a variety of airborne δD in-situ measurements (for more details please refer to Schneider et al., 2006b).

The retrievals are performed in four different spectral regions: 790–880, 1090–1330, 2650–3180, and 4560–4710 cm^{-1}. The fitted spectral microwindows containing the water vapour lines are shown in Figs. 1–4, which show a typical ground-based MkIV MOHAVE-2009 measurement of a solar absorption spectrum with a spectral resolution of about 0.008 cm^{-1} (OPDmax = 116.5 cm). In the 790–880 cm^{-1} region the $H_2^{16}O$ lines are well isolated from other absorbers but relatively strong and consequently often saturated in ground-based solar absorption spectra. In the 1090–1330 cm^{-1} region we can fit both $H_2^{16}O$ and $HD^{16}O$ lines. The former are often saturated and in addition interfere with O_3 absorption signatures whereas the latter interfere mainly with CH_4 signatures. In order to avoid significant interference errors (Sussmann and Borsdorff, 2007) it is important to simultaneously retrieve O_3, CH_4 as well as N_2O profiles. The 2650–3180 cm^{-1} region contains well isolated lines of $H_2^{16}O$, $H_2^{18}O$, and $HD^{16}O$, which are generally not saturated. The 4560–4710 cm^{-1} region contains well isolated and not saturated $H_2^{16}O$ lines.

In addition to the water vapour lines shown in Figs. 1–4, we fit for all retrievals several CO_2 lines of different strength, which allows us to optimally estimate the temperature from the measured spectra (Schneider and Hase, 2008). As a priori temperature profile we use reanalysis data from the National Centers for Environmental Prediction (NCEP). As temperature uncertainty covariance we assume an uncertainty correlation length of 10 km (excluding the boundary layer) and uncertainty values of 2 K in the boundary layer, 1 K throughout the rest of the troposphere, and 5 K above the tropopause.

Due to the large vertical gradient and the large dynamic range of tropospheric water vapour amounts, ground-based water vapour retrievals are very demanding. In order to produce data of good quality we apply the sophisticated recipes presented in Schneider and Hase (2009b). These are: (a) a fit to a variety of water vapour lines with different strength, (b) a logarithmic scale inversion, (c) a speed-dependent Voigt line-shape model, (d) a simultaneous temperature profile retrieval, and (e) the consideration of atmospheric emission for the retrievals at low wavenumbers. For the retrievals in the 1090–1330 and 2650–3180 cm^{-1} regions we introduce an $H_2^{16}O$–$HD^{16}O$ and $H_2^{16}O$–$H_2^{18}O$ inter-species constraint. This inter-species constraint is mandatory for an optimal estimation of δD profiles (Schneider et al., 2006b) and of $\delta^{18}O$ column integrated values.

As spectral parameters for the line-by-line modelling we use the HITRAN 2008 parameters (Rothman et al., 2009, with 2009 updates). We slightly modified the $H_2^{16}O$ and $HD^{16}O$ parameters in the 790–1330 cm^{-1} range in order to minimize the systematic differences between simulated and measured signatures: a modification of 1–2 % of the pressure broadening coefficients γ_{air} and of line strength coefficients S of less than 5% (Schneider and Hase, 2009a). These modifications are all within the uncertainty ranges given in the

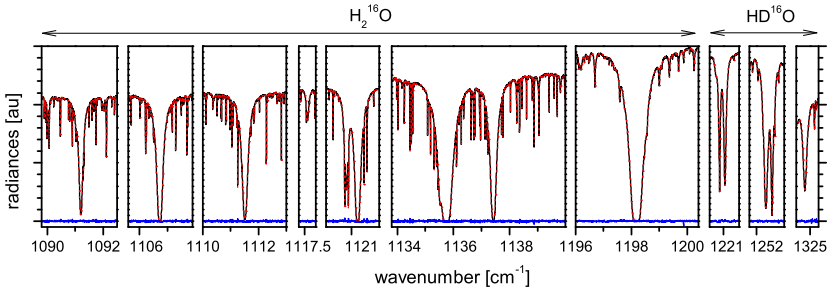

Fig. 2. Same as Fig. 1 but for the 1090–1330 cm^{-1} retrieval.

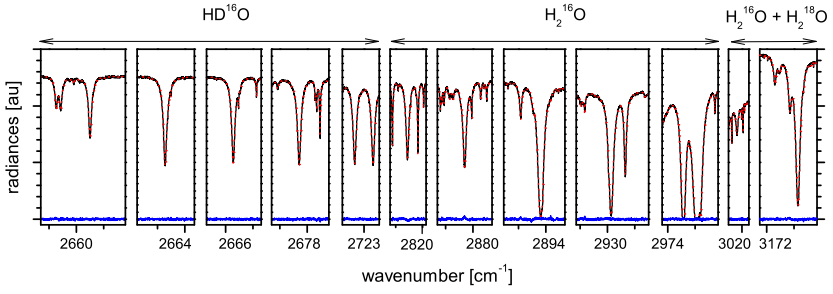

Fig. 3. Same as Fig. 1 but for the 2650–3180 cm^{-1} retrieval.

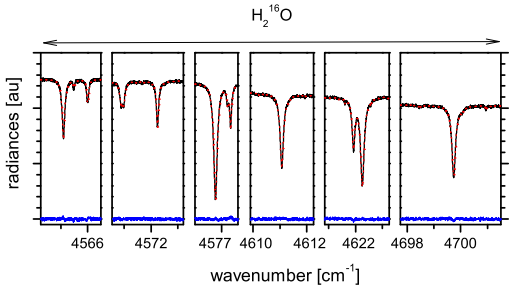

Fig. 4. Same as Fig. 1 but for the 4560–4710 cm^{-1} retrieval.

HITRAN parameter file. Furthermore, we adjusted the line parameters for a speed-dependent Voigt line-shape model, since different laboratory studies clearly reveal the superiority of the speed-dependent Voigt line shape model over the commonly applied Voigt line shape model when simulating high resolution spectra in the infrared (e.g., D'Eu et al., 2002; Tran et al., 2007; Wagner and Birk, 2009). In addition Schneider and Hase (2009a) and Schneider et al. (2010c) demonstrate that applying a speed-dependent Voigt instead of a Voigt line shape model is strongly recommended for ground-based water vapour profile remote sensing in the infrared. For further details about adjusting the HITRAN line parameters for speed-dependence please refer to Schneider et al. (2010c).

4 Theoretical performance

4.1 Vertical resolution and sensitivity

Figure 5 shows the averaging kernels for H_2O for the four regions and for the typical measurement as shown in Figs. 1–4. All four spectral regions offer a similar vertical resolution with respect to tropospheric H_2O. Structures with a width of 3, 6, and 10 km (full width at half maximum of the kernels) can be detected for the lower, middle, and upper troposphere, respectively. The sensitivity (sum along the row of the averaging kernel matrix, black line in Fig. 5) quantifies the influence of the measured spectra on the retrieved mixing ratio profiles, as opposed to the a priori constraint. There are small differences concerning the sensitivity: for the 790–880 and the 1090–1330 cm^{-1} region the sensitivity is better than 75% for altitudes below 11 km. For the 2650–3180 and 4560–4710 cm^{-1} this sensitivity range is extended by about 1 km to higher altitudes. The reason for this differences is the application of rather strong lines in the two low wavenumber regions. The saturated or almost saturated lines provide less information about absorptions at high altitudes.

Figure 6 depicts the averaging kernels of δD for the mid-infrared retrievals at 1090–1330 and 2650–3180 cm^{-1}. Both spectral regions offer a similar vertical resolution and sensitivity. The natural δD variability is rather small (about 8%). It is difficult to correctly interpret the spectral signatures caused by such small variability and as a consequence the profiles of δD are much more difficult to measure than profiles of H_2O. The vertical resolution is limited to about 3 km for the lower troposphere and 10 km for the middle/upper

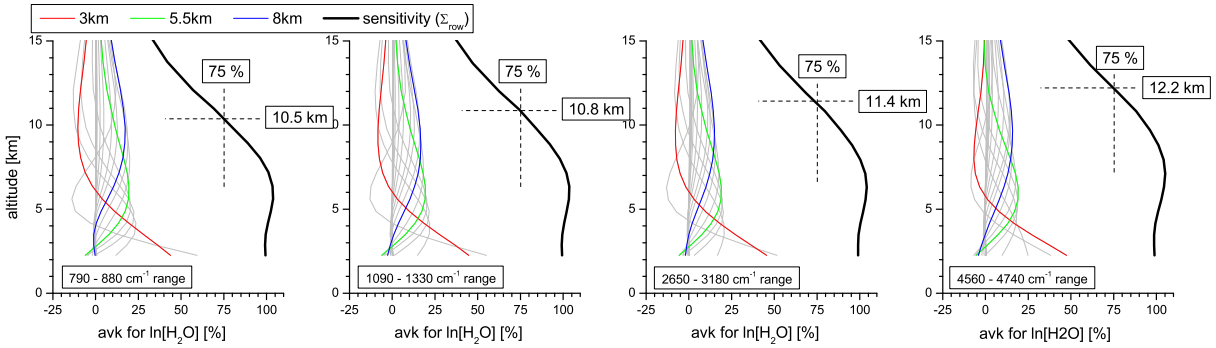

Fig. 5. Averaging kernels for ln[H_2O] for the four analysed spectral regions. Grey lines: kernels for all atmospheric model grid levels; Red, green, and blue lines: kernels for the 3, 5.5, and 8 km grid level (representative for the lower, middle, and upper troposphere), respectively; Thick black line: Sensitivity (sum along the row of the averaging kernel matrix).

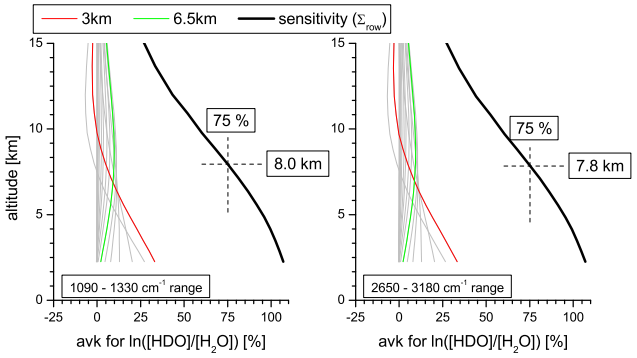

Fig. 6. Averaging kernels for δD (expressed as $\ln\frac{[HDO]}{[H_2O]}$) for the mid-infrared spectral regions. Grey lines: kernels for all atmospheric model grid levels; Red and green lines: kernels for the 3 and 6.5 km grid level (representative for the lower and middle/upper troposphere); Thick black line: Sensitivity (sum along the row of the averaging kernel matrix).

troposphere. The sensitivity is larger than 75% only for altitudes below about 8 km.

The trace of the averaging kernel matrix quantifies the amount of information introduced by the measurement. It can be interpreted in terms of degrees of freedom of the measurement (dof). The larger this value the more independent the solution is from the a priori assumptions. Table 1 collects the typical dof values for the retrievals in the different spectral regions. In the 1090–1330 and 2650–3180 cm^{-1} regions we retrieve several water vapour isotopologues. There the typical overall water vapour dof value is about 4.1–5.2 compared to 2.6 in case of the 790–880 and 4560–4710 cm^{-1} regions, where we only retrieve the main isotopologue $H_2^{16}O$.

The limitations in vertical resolution and sensitivity are also reflected in the retrieved column integrated values. We estimate this so-called smoothing error as follows: we simulate spectra for a variety of different vertically highly-resolved H_2O profiles (as δD we assume a constant -200‰ value for all altitudes). Subsequently, we invert the simulated spectra and calculate the differences between the retrieved column integrated values and the original column integrated values. The standard deviations of these differences are the random smoothing errors. They are collected in Table 2 for the different retrievals. They are about 0.5% for column integrated H_2O and about 2‰ for column integrated δD.

Table 1. Typical degree of freedoms (dof) with respect to water vapour for the measurements in the different spectral regions.

spectral range	dof	isotopologues
790–880 cm^{-1}	2.6	$H_2^{16}O$
1090–1330 cm^{-1}	4.1	$H_2^{16}O$, $HD^{16}O$
2650–3180 cm^{-1}	5.2	$H_2^{16}O$, $H_2^{18}O$, $HD^{16}O$
4560–4710 cm^{-1}	2.6	$H_2^{16}O$

4.2 Propagation of uncertainty sources

In this section we estimate the errors of the H_2O and δD profiles for each of the four different retrievals. The estimation is based on the assumed uncertainty sources as listed in the Tables 3 and 4.

Concerning experimental uncertainties we assume a measurement noise of 0.5% (defined as noise to signal ratio). Furthermore, we consider an instrumental line shape (ILS: modulation efficiency and phase error) and a baseline offset uncertainty. During the MOHAVE-2009 campaign we made regular low pressure gas cell measurements in order to monitor the actual ILS applying the LINEFIT software Hase et al. (1999). LINEFIT estimates the modulation efficiency and the phase error at 20 equidistant optical path intercepts. These estimations were taken into account for all our calculations. All LINEFIT estimations during MOHAVE-2009 were consistent within less than 5% (for the modulation

Table 2. Smoothing error of the column integrated values for the retrievals in the different spectral regions.

spectral range	H_2O	δD
790–880 cm^{-1}	0.6%	–
1090–1330 cm^{-1}	0.3%	1.5‰
2650–3180 cm^{-1}	0.4%	2.8‰
4560–4710 cm^{-1}	0.6%	–

Table 3. Assumed experimental and temperature random uncertainty.

source	uncertainty
measurement noise	0.5%
phase error	0.01 rad
modulation eff.	5%
baseline offset	0.5%
LT temperature	2 K
UT temperature	2 K

efficiency) and 0.01 rad (for the phase error) and we use these values as the ILS uncertainty. Baseline offsets might be produced by detector non-linearities. In analogy to other studies (Schneider and Hase, 2008) we assume a baseline offset uncertainty of 0.5% (defined as ratio between the offset intensity and the signal, i.e. the intensity outside of absorption signatures). In addition to instrumental deficits high cirrus clouds might disturb the ILS and/or be responsible for baseline offsets (due to intensity fluctuation during the interferometer scans).

For the radiative transfer calculation we need to know the actual temperature profile. We use the National Centers for Environmental Prediction (NCEP) automailer system which provides daily reanalysis temperatures. The reanalysis data might be subject to uncertainties and furthermore they might not well represent small scale features like the local diurnal cycle above TMF, i.e., they might differ from the actual temperature during the FTIR measurement. We assume an uncertainty of 2 K for the lower troposphere (LT: below 5 km) and 2 K for the upper troposphere (UT: above 5 km).

The line-by-line modelling relies on the parameters collected in spectroscopic databases like HITRAN (Rothman et al., 2009). Here we consider an uncertainty in the line strength (S), the air pressure broadening coefficient (γ_{air}), and the line shape model (strength of speed-dependence: Γ_2/Γ_0, D'Eu et al., 2002), which are the parameters whose uncertainty has the strongest effect on the retrieved H_2O and δD profiles. The HITRAN file gives parameter uncertainty values for S and γ_{air} of about 1–5%. In Schneider and Hase (2009a) and Schneider et al. (2010c) we optimised this parameters and assume for our estimation an uncertainty of $+1$ and $+2$% (for $H_2^{16}O$ and $HD^{16}O$, respectively). For the strength of the speed-dependence we assume an uncertainty of $+5$ and $+10$% (for $H_2^{16}O$ and $HD^{16}O$, respectively). We assume different uncertainties for $H_2^{16}O$ and $HD^{16}O$ since inconsistencies between the $H_2^{16}O$ and $HD^{16}O$ line parameters are a major error source for δD profiles remotely-sensed from ground (Schneider et al., 2006b).

The measurement noise error matrix is estimated by $\mathbf{S} = \mathbf{G}\mathbf{S_y}\mathbf{G}^T$ (Rodgers, 2000), whereby $\mathbf{G}$ and $\mathbf{S_y}$ are the gain matrix and the measurement noise matrix, respectively. All the other errors are determined by a full treatment. Therefore,

Table 4. Assumed spectroscopic parameter uncertainty for $H_2^{16}O$ and $HD^{16}O$.

source	$H_2^{16}O$	$HD^{16}O$
line strength, S	$+1$%	$+2$%
pres. broad. coef., γ_{air}	$+1$%	$+2$%
SDV strength, Γ_2/Γ_0	$+5$%	$+10$%

we use an ensemble of spectra measured for different atmospheric $H_2^{16}O$ and δD states that are representative for the typical mean and variability (actually we use the spectra corresponding to the the seven $H_2^{16}O$ profiles shown later in Fig. 11). We perform two retrievals: a first with a correct parameter and a second with an erroneous parameter (e.g., introduction of a baseline offset of 0.5%, by 2 K increased lower tropospheric temperature, application of a 1% higher $H_2^{16}O$ line strength parameter). The systematic and the random error are then given by the mean and the standard deviation of the difference between the two retrievals. This method also allows estimating random errors of systematic uncertainty sources: the spectroscopic parameters are systematic uncertainties but the effect of this uncertainty depends on the actual sensitivity of the remote sensing system, which is different for dry and wet atmospheric conditions. Consequently, a systematic uncertainty source can cause random errors.

Figures 7 and 8 show the random and systematic errors for the H_2O profiles for each of the four retrievals and Figs. 9 and 10 the same but for δD and for the two retrievals in the 1090–1330 and 2650–3180 cm^{-1} region. We combine the error due to a misalignment of the instrument (modulation efficiency error and phase error) as the instrumental line shape (ILS) error. Errors due to lower and upper tropospheric temperature uncertainty are combined as the temperature error and the random error caused by the systematic uncertainty of the different spectroscopic parameters (S, γ_{air}, Γ_2/Γ_0) is merged to a single spectroscopic random error.

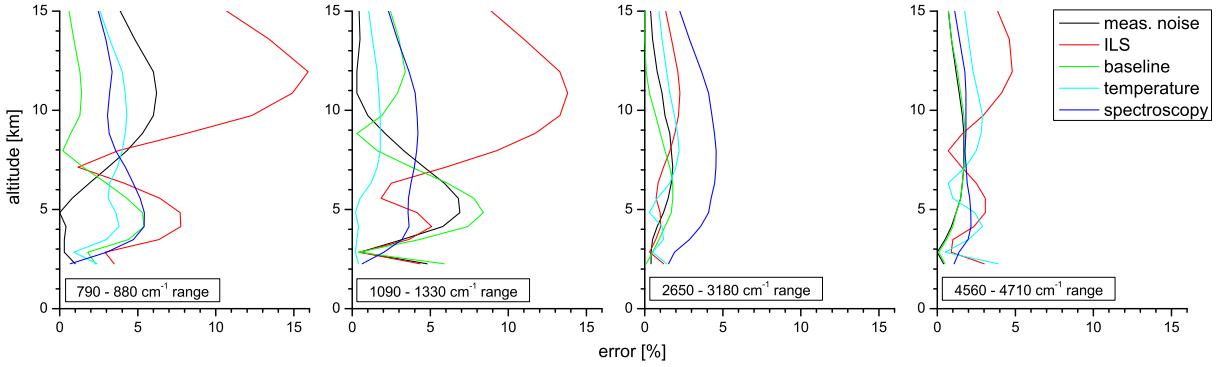

Fig. 7. Estimated H_2O random profile errors for the retrievals in the four different spectral regions. Black: measurement noise; Red: ILS; Green: baseline offset; Cyan: temperature profile; Blue: spectroscopic parameters.

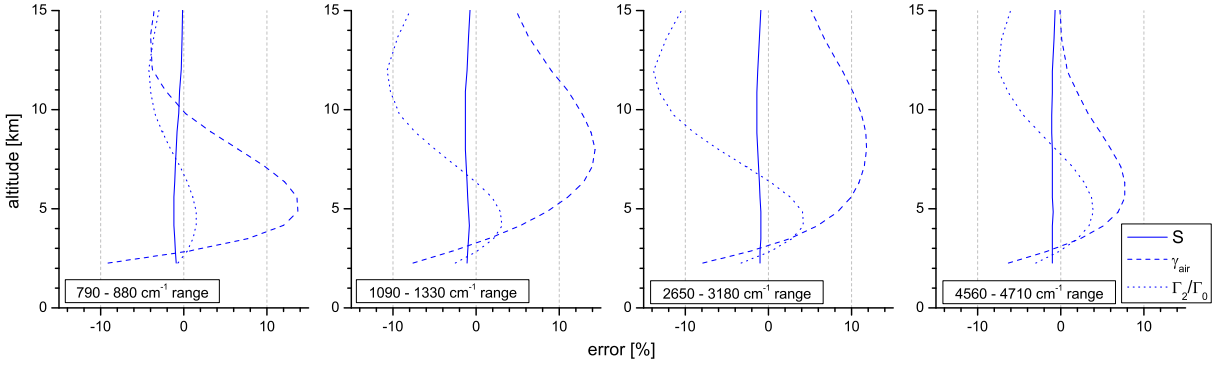

Fig. 8. Estimated H_2O systematic profile errors for the retrievals in the four different spectral regions. Solid line: line strength (S) uncertainty; Dashed line: pressure broadening coefficient (γ_{air}) uncertainty; Dotted line: speed-dependence strength (Γ_2/Γ_0) uncertainty.

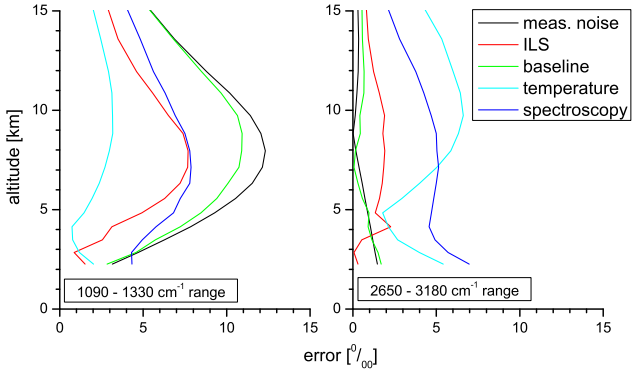

Fig. 9. Same as Fig. 7 but for δD and the two retrievals at 1090–1330 and 2650–3180 cm^{-1}.

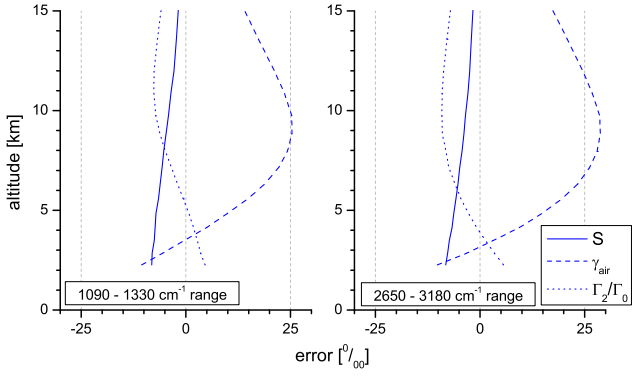

Fig. 10. Same as Fig. 8 but for δD and the two retrievals at 1090–1330 and 2650–3180 cm^{-1}.

4.2.1 H_2O errors

Our estimation reveals that the H_2O profiles inverted from signatures in the low wavenumber regions (790–880 and 1090–1330 cm^{-1}) are theoretically less precise than the profiles of the high wavenumber regions (see Fig. 7). At the low wavenumbers we apply several rather strong and often saturated lines. Then the measurement noise as well as the ILS and baseline offset uncertainties have a significant impact on the retrieved profiles. This difference to high wavenumber retrievals is actually even more pronounced than indicated by Fig. 7: for the depicted estimation we assumed the same

Table 5. Estimated random errors of column integrated $H_2^{16}O$ for retrievals in different spectral regions.

source	790–880 cm^{-1}	1090–1330 cm^{-1}	2650–3180 cm^{-1}	4560–4710 cm^{-1}
measurement noise	1.3%	0.6%	0.7%	0.4%
ILS	0.4%	0.8%	0.1%	0.1%
baseline offset	1.0%	1.5%	0.8%	0.6%
temperature	0.4%	0.1%	0.2%	<0.1%
spectroscopy	0.1%	0.2%	0.1%	<0.1%

Table 6. Estimated random errors of column integrated δD for retrievals in different spectral regions.

source	1090–1330 cm^{-1}	2650–3180 cm^{-1}
measurement noise	6.3‰	1.1‰
ILS	3.2‰	0.7‰
baseline offset	6.6‰	1.3‰
temperature	0.6‰	1.8‰
spectroscopy	1.8‰	1.6‰

noise to signal and baseline offset to signal ratio over the whole spectral range. However, at low wavenumbers the intensity of the solar radiation is actually smaller than at high wavenumbers resulting in increased noise to signal and offset to signal ratios at low wavenumbers. Furthermore, the assumption of a 0.5% baseline offset at high wavenumbers is very likely exaggerated: an important cause of these offsets are detector non-linearities, which are typical for the HgCdTe photoconductor (applied for wavenumbers below 1850 cm^{-1}) but not for the InSb photodiode (applied for recording high wavenumbers).

For the 2650–3180 cm^{-1} retrieval the systematic uncertainty in the spectroscopic parameters are the leading random error source. The spectroscopic uncertainty is equally important for the 4560–4710 cm^{-1} retrieval. Note that the 2650–3180 cm^{-1} error only appears larger due to our large $HD^{16}O$ uncertainty assumption and the $HD^{16}O$–$H_2^{16}O$ interspecies constraint: the assumed $HD^{16}O$ uncertainties double the assumed $H_2^{16}O$ uncertainties (see Table 4) and by constraining $H_2^{16}O$ against $HD^{16}O$ we link the 2650–3180 cm^{-1} $H_2^{16}O$ profile errors to the relatively large $HD^{16}O$ uncertainty assumptions.

The $HD^{16}O$–$H_2^{16}O$ interspecies constraint has also to be considered when interpreting the systematic $H_2^{16}O$ error estimations (Fig. 8). For the 1090–1330 and 2650–3180 cm^{-1} retrieval the $H_2^{16}O$ errors are in particular large due to the link to the large $HD^{16}O$ uncertainty assumptions. Uncertainties in the parameters that describe the line shape (γ_{air} and Γ_2/Γ_0) can produce systematic $H_2^{16}O$ profiles errors of up to 15%.

Table 5 collects the estimated random errors of the retrieved $H_2^{16}O$ column abundances. The column abundance error can reach 1.5–2% for the low wavenumber retrievals (due to measurement noise and baseline offset uncertainties) and is generally below 1% for the high wavenumber retrievals. The systematic column abundance errors are dominated by the error due to the line strength uncertainty. It is about -1% for the assumed $+1$% line strength uncertainty.

4.2.2 δD errors

Similar to the $H_2^{16}O$ we find that the high wavenumber retrievals produce theoretically more precise δD profiles than the low wavernumber retrievals. Figure 9 documents that for the 1090–1330 cm^{-1} retrieval the measurement noise and the baseline offset uncertainties have significant impacts on the δD profiles. For the 2650–3180 cm^{-1} retrieval these error sources can almost be neglected, in particular if we consider that for high wavenumbers the measurement noise and baseline offset error assumptions of Table 3 are very likely exaggerated (see discussion of H_2O errors). In the 2650–3180 cm^{-1} region the spectroscopic parameter and temperature profile uncertainties are most important. For δD, i.e. $HD^{16}O/H_2^{16}O$, inconsistencies between the $H_2^{16}O$ and $HD^{16}O$ parameters are responsible for the spectroscopic errors (an uncertainty consistent for $H_2^{16}O$ and $HD^{16}O$ would cause almost no error in the retrieved $HD^{16}O/H_2^{16}O$). The increased importance of the temperature uncertainty of the 2650–3180 cm^{-1} retrieval if compared to 1090–1330 cm^{-1} retrieval is caused by the rather weak CO_2 signatures around 2620 cm^{-1} that are used for retrieving the temperature. In the low wavenumber region we can apply rather strong and isolated CO_2 signatures around 960 cm^{-1} to reduce the temperature error.

The systematic errors are very similar for both spectral regions and can reach 30‰, in the middle/upper troposphere.

The estimated random errors of the column integrated δD values are collected in Table 6. For the 1090–1330 cm^{-1} retrieval measurement noise and baseline offset uncertainty are significant error sources. The 2650–3180 cm^{-1} retrieval provides theoretically more precise column integrated δD data than the 1090–1330 cm^{-1} retrieval, whereby the temperature uncertainty is the most important error source. The systematic errors for column integrated δD are dominated by a potential inconsistency between the $H_2^{16}O$ and $HD^{16}O$ line

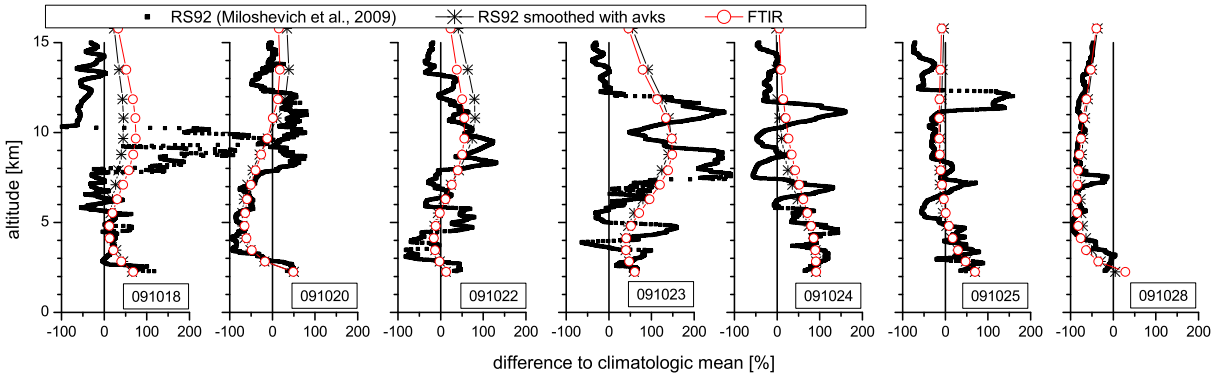

Fig. 11. Comparison of the seven coincident FTIR and Vaisala RS92 H_2O measurements made during MOHAVE-2009 (18th, 20th, 22nd, 23rd, 24th, 25th, and 28th of October 2009). Profiles are presented as percentage difference to a subtropical climatological profile, FTIR profiles are for a retrieval in the 2650–3180 cm^{-1} region. Black squares: RS92 data corrected by the Miloshevich et al. (2009) method; Black stars: RS92 smoothed with FTIR averaging kernels; Red circles: FTIR.

strength parameters. For the assumed inconsistency of 1% it is about 7.5‰ for both retrievals.

5 H_2O profiles

During MOHAVE-2009 many radiosondes were launched. Although most launches were during night (in order to coincide with the lidar measurements) there were seven Vaisala RS92 measurements performed at the same time as MkIV measurements. The sondes were launched about 350 m from the location of the spectrometer. Therefore, the coincident RS92 in-situ and the MkIV remote sensing experiments detect a very similar airmass, at least at low altitudes.

Figure 11 compares the 7 coincident RS92 and MkIV H_2O profiles (for the 2650–3180 cm^{-1} retrieval): the small black squares show the RS92 profiles after the so-called time-lag, radiation, and empirical corrections were applied (Miloshevich et al., 2004, 2009). These in-situ profiles offer a very high vertical resolution. In contrast, the remote sensing technique only allows resolving rather rough vertical structures (see averaging kernels of Fig. 5). For an adequate comparison we have to degrade the RS92 profiles to the vertical resolution of the MkIV profiles. Therefore, we convolve the vertically highly-resolved RS92 profiles (x_{RS92}) with the FTIR averaging kernels $\hat{\mathbf{A}}$:

$$\hat{x}_{RS92} = \hat{\mathbf{A}}(x_{RS92} - x_a) + x_a \quad (1)$$

The result is a smoothed RS92 profile ($\hat{x}_{RS92}$) with the same vertical resolution as the FTIR profile (x_a in Eq. (1) stands for the a priori climatological mean profile). The black stars in Fig. 11 depict these $\hat{x}_{RS92}$ profiles. Their comparison to the vertically highly-resolved profiles (black squares) gives a good impression about the vertical H_2O structures that can be resolved by the ground-based FTIR remote sensing technique: a ground-based FTIR system is able to detect the relatively large water vapour amount between 7 and 12 km on day 091023 but its vertical resolution is too rough for reproducing the sharp maximum at 11.5 km on day 091025. The red circles represent the profiles as retrieved from the MkIV spectra in the 2650–3180 cm^{-1} region. Figure 11 shows the difference to the climatologic mean, which is used as the a priori profile. Therefore, any deviation with respect to the depicted 0% line is produced by the measurement. The good agreement between the FTIR and the smoothed RS92 profiles reveals the capability of the FTIR system to capture the large dynamic of tropospheric water vapour and to distinguish between lower and upper tropospheric humidity.

Figure 12 summarizes the RS92-MkIV H_2O profile comparisons. It depicts the differences between the FTIR and smoothed RS92 profiles (difference between red circles and black stars of Fig. 11) for all four spectral region. Generally the 1σ scatter between RS92 and MkIV is smaller than 20% (defined as $2 \times \frac{FTIR-RS92}{FTIR+RS92}$). An exception is the 790–880 cm^{-1} retrieval where it reaches 35%. The apparently poorer precision of the low wavenumber retrieval is in qualitative agreement with the theoretical error estimation (see Fig. 7). The large relative difference between FTIR and RS92 on 091028 is similar for all retrievals and dominates the scatter RS92-MkIV scatter values. On this day the troposphere is very dry (compare Fig. 11) and the observation of a slightly more humid airmass by the RS92 if compared to the FTIR can be responsible for this outlier.

For all four retrievals the mean difference to the sonde (thick grey line) is smaller than 10% throughout the troposphere, an exception is the boundary layer value for the 790–880 cm^{-1} retrieval, which deviates systematically by 14% from the RS92 value. Please note that such good agreement is only achieved by applying the line parameters adjusted for speed-dependence as described in Schneider et al. (2010c).

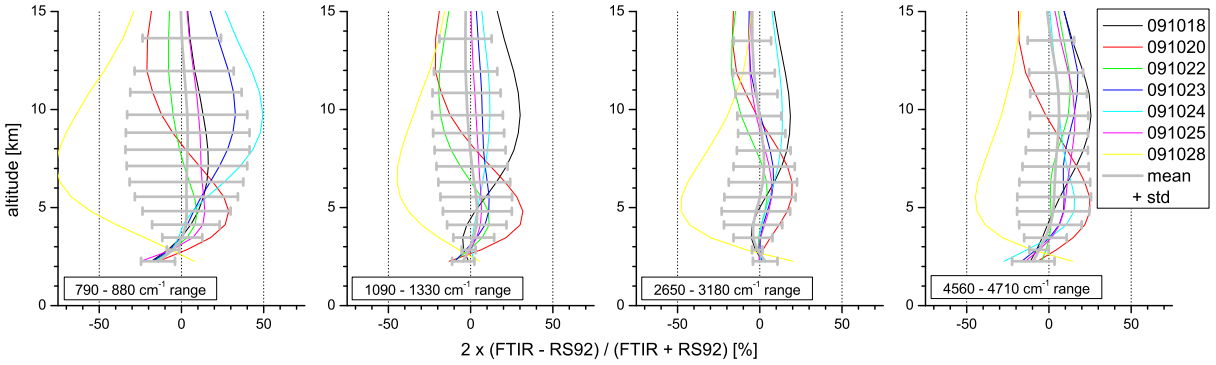

Fig. 12. Difference between coincident FTIR and smoothed RS92 H_2O profiles for the retrievals in the four spectral regions. Coloured lines: individual coincidences; Thick grey line and error bars: mean and standard deviation.

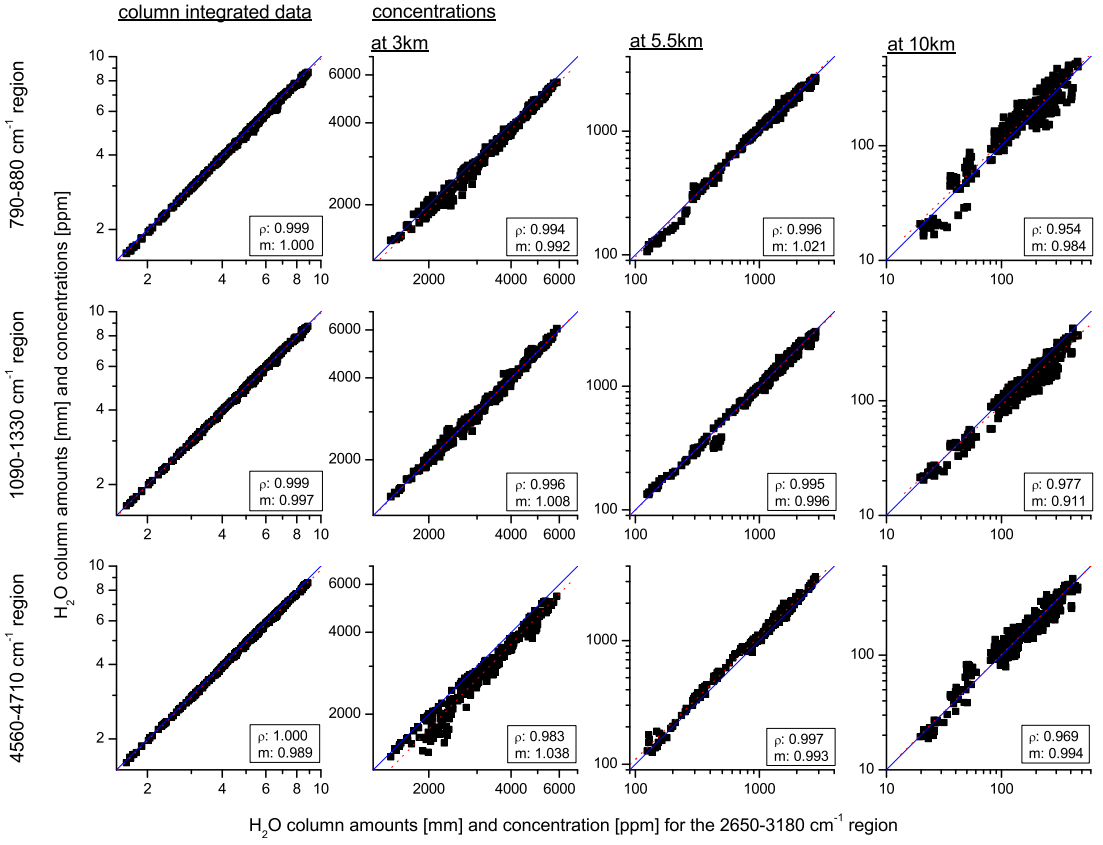

Fig. 13. Correlation between the 325 H_2O profile retrieved for the different spectral regions. Top panels: 790–880 cm^{-1} region (y-axes) versus 2650–3180 cm^{-1} region (x-axis); Central panel: 1090–1330 cm^{-1} region (y-axes) versus 2650–3180 cm^{-1} region (x-axis); Bottom panels: 4560–4710 cm^{-1} region (y-axes) versus 2650–3180 cm^{-1} region (x-axis). From left to right: total column amounts (in mm), volume mixing ratios (in ppm) for the lower, middle, and upper troposphere (3, 5.5, 10 km, respectively). The blue solid line indicates the diagonal and the red dotted line the linear regression line. The correlation coefficient ρ and the slope of the linear regression line m are written in each panel.

Concerning H_2O column abundances we find for all retrievals a very similar good agreement to the RS92. The scatter is about 7.5% and the systematic difference is situated between −2.4 and −0.1% (see Table 7).

During MOHAVE-2009 325 spectra were measured on 11 different days. We made 325 retrievals in each of the four spectral regions and analysed their consistency. Figure 13 shows the correlations between the column integrated

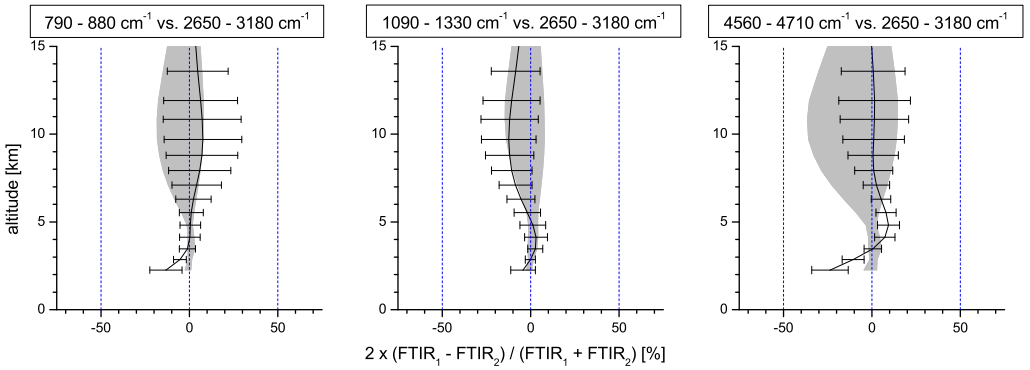

Fig. 14. Difference between the H_2O profiles retrieved in different spectral regions. Left panel: difference between 790–880 and 2650–3180 cm^{-1} region; Central panel: difference between 1090–1330 and 2650–3180 cm^{-1} region; Right panel: difference between 4560–4710 and 2650–3180 cm^{-1} region. Black line and error bars mean: 1σ standard deviation of the differences between the 325 retrievals; Grey area: Theoretical differences due to different averaging kernels; see Eq. (2).

Table 7. Difference (mean and standard deviation) between coincident FTIR and RS92 H_2O column abundances for the retrievals in the four spectral regions.

spectral range	$2\times\frac{\text{FTIR}-\text{RS92}}{\text{FTIR}+\text{RS92}}$
790–880 cm^{-1}	$-2.4\pm7.5\%$
1090–1330 cm^{-1}	$-0.5\pm7.5\%$
2650–3180 cm^{-1}	$-0.1\pm7.2\%$
4560–4710 cm^{-1}	$-2.2\pm7.2\%$

amounts as well as the lower, middle, and upper tropospheric concentrations obtained by the 325 retrievals in the three spectral regions. For this study we take the 2650–3180 cm^{-1} retrieval as the reference retrieval. The top panels show the correlations between the 790–880 and 2650–3180 cm^{-1} retrievals, the central panel between the 1090–1330 and 2650–3180 cm^{-1} retrievals, and the lower panel between the 4560–4710 and 2650–3180 cm^{-1} retrievals. The correlations are very strong (coefficients ρ are close to 1 throughout the troposphere). Figure 13 proves that the water vapour profiles and total column abundances obtained in the four different spectral regions are very consistent. In all three spectral regions the FTIR system observes almost identical lower, middle, and upper tropospheric water vapour variations.

In Fig. 14 we depict statistics of the differences between the different water vapour retrievals. The left panel shows the mean and 1σ standard deviation (black line and error bars) of difference between the 790–880 and 2650–3180 cm^{-1} retrievals. The mean difference is smaller than 7% throughout the troposphere (except for the boundary layer where it reaches 13%) and the scatter is smaller than 22%. When comparing two remotely-sensed profiles we have to account for differences in the averaging kernels. The H_2O averaging kernels of the 790–880 and 2650–3180 cm^{-1} retrievals are similar but not identical (see Fig. 5). With statistics of the differences between the real state x and the climatological mean state x_a represented by the ensemble $\{x-x_a\}$ we can estimate how the differences in the averaging kernels affects our comparison:

$$\{\epsilon_1-\epsilon_2\}=(\hat{\mathbf{A}}_\mathbf{1}-\hat{\mathbf{A}}_\mathbf{2})\{x-x_a\} \quad (2)$$

Here $\hat{\mathbf{A}}_\mathbf{1}$ and $\hat{\mathbf{A}}_\mathbf{2}$ are typical averaging kernels for the 790–880 and the 2650–3180 cm^{-1} retrieval, respectively. The ensemble $\{\epsilon_1-\epsilon_2\}$ represents the expected differences between the two retrievals caused by the different averaging kernels (see also Rodgers and Connor, 2003). The grey areas in the graphs of Fig. 14 represent the 1σ area of the ensemble $\{\epsilon_1-\epsilon_2\}$. We observe that a large part of the scatter between the two different H_2O retrievals can be explained by the averaging kernels.

However there are systematic differences that cannot be explained by the averaging kernels: increased difference between the lower tropospheric amounts obtained from the 4560–4710 and 2650–3180 cm^{-1} retrievals or between the middle/upper tropospheric amounts retrieved from the 1090–1330 and the 2650–3180 cm^{-1} retrievals. They are very likely due to inconsistencies between the spectroscopic line parameters of the different spectral regions.

Table 8 informs about the very good consistency between the H_2O column abundances obtained from retrievals in the different spectral regions. Taking the 2650–3180 cm^{-1} retrieval as the reference we observe biases between -1.0 and -2.7% and scatter values of about 1%. The relative systematic differences obtained from the big ensemble of 325 retrievals well confirms the values obtained from the comparison for the 7 RS92 coincidences (see Table 7).

Table 8. Difference (mean and standard deviation) between the H_2O column abundances obtained in the different spectral regions taking the 2650–3180 cm^{-1} retrieval as the reference (REF).

spectral range (X)	$2 \times \frac{X-REF}{X+REF}$
790–880 cm^{-1}	$-2.3 \pm 1.1\%$
1090–1330 cm^{-1}	$-1.0 \pm 1.2\%$
4560–4710 cm^{-1}	$-2.7 \pm 1.0\%$

6 δD profiles

Besides the ground-based FTIR there is no other MOHAVE-2009 experiment with the capability to measure tropospheric δD profiles. So we cannot perform a comparison as shown in Figs. 11 and 12 for the H_2O profiles. Instead we compare statistics. The grey area in Fig. 15 represents the 1σ range of subtropical δD in-situ measurements performed by Ehhalt (1974) and Zahn (2001). Superimposed are statistics of δD as retrieved from the MOHAVE-2009 MkIV spectra. The red line shows the mean and the 1σ standard deviation for all the 325 δD profiles retrieved in the 790–1330 cm^{-1} region, the blue line and error bars show the same but for the 2650–3180 cm^{-1} retrievals. In both spectral regions we observe a monotonic decrease of δD values between the lower and upper troposphere, which is in good agreement with the profiles obtained by different in-situ measurements.

In Fig. 16 we depict correlations between the δD values obtained by the retrievals in the two mid-infrared spectral regions. The agreement is very satisfactory. Please keep in mind that the axis are in the ‰, scale, i.e. Fig. 16 shows variations of a few percent only. Such small variations are very challenging for a remote sensing system. Nevertheless, we observe that for both spectral regions the same small variations in δD are detected. Keeping in mind that uncertainties in the spectroscopic parameters and measurement noise are leading error sources for ground-based δD remote sensing, the strong correlation between the δD profiles retrieved in two different spectral regions is a nice demonstration of the quality of these profiles.

Figure 17 shows the mean and standard deviation for the 325 δD profiles retrieved in the two mid-infrared regions. The 1σ standard deviation is about 10‰ in the lower troposphere and reaches 22‰ in the upper troposphere (at 9 km). A part of these scatter is due to differences in the vertical resolution and sensitivity of the two retrievals. The grey area shows the estimation according to Eq. (2). Removing the scatter caused by the different averaging kernels leaves a scatter of about 8 and 17‰ for the lower and middle/upper troposphere, respectively. The leading error sources of ground-based FTIR δD profiles are measurement noise and deficits in the spectroscopic line parameters. These errors are uncorrelated for the two retrievals, therefore the observed 8 and 17‰ scatter can be interpreted as an upper

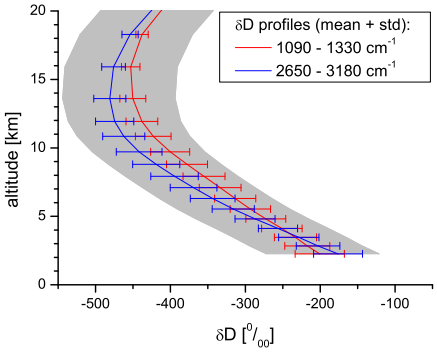

Fig. 15. Statistics of subtropical δD profiles: Grey area: 1σ range of δD measured typically in the subtropics (Ehhalt, 1974; Zahn, 2001); Lines and error bars: mean and 1σ standard deviation of the 325 MOHAVE-2009 FTIR retrievals; Red: in the 1090–1330 cm^{-1} region; Blue: in the 2650–3180 cm^{-1} region.

estimate of the FTIR's lower and middle/upper tropospheric δD precision (it can be interpreted as the sum of the random errors from both retrievals).

However, the mean difference between the two δD retrievals is significant, in particular in the middle/upper troposphere where it reaches 40‰. This cannot be explained by the different averaging kernels. Instead it is very likely due to remaining inconsistency between the spectroscopic $H_2^{16}O$ and $HD^{16}O$ line parameters, for which the retrieved δD profiles are very sensitive (see Fig. 10 and Schneider et al., 2006b).

Concerning column integrated δD we observe a difference (mean and standard deviation) of 2.6 ± 9.3‰ between the two retrievals.

7 Conclusions

We show that tropospheric H_2O and δD profiles can be obtained from infrared solar absorption spectra recorded in different spectral regions. The mid-infrared regions (790–880, 1090–1330, and 2650–3180 cm^{-1}) are measured regularly by the NDACC ground-based FTIR spectrometers, whereas the near infrared region (4560–4710 cm^{-1}) is covered by the TCCON spectrometers (although with a spectral resolution limited to 0.02 cm^{-1}). Concerning H_2O all four spectral regions allow a distinction between lower, middle, and upper tropospheric water vapour according to the averaging kernels of Fig. 5. When adjusting the line parameters for speed-dependance the 1σ scatter between the FTIR and RS92 profiles measured in coincidence during the MOHAVE-2009 campaign is generally smaller 20%, except for the 790–880 cm^{-1} retrieval where it is poorer. The different water vapour profiles are very consistent. Taking into account the different averaging kernels the scatter between the retrievals is very likely smaller than 10% throughout the troposphere. We observe some systematic differences with respect to the

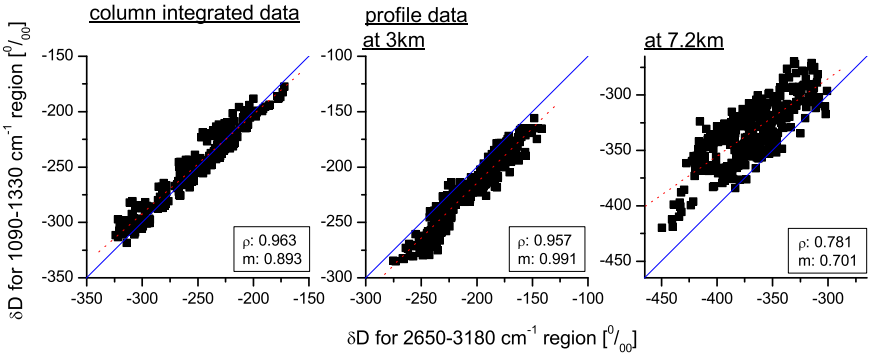

Fig. 16. Same as top panels of Fig. 13 but for δD profile retrievals and for column integrated, lower, and middle/upper tropospheric δD (3 and 7.2 km, respectively)

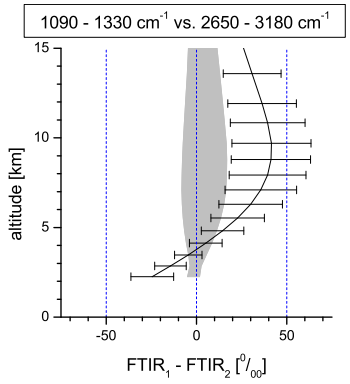

Fig. 17. Same as Fig. 14, but for δD profiles retrieved in the 1090–1330 and 2650–3180 cm^{-1} regions.

radiosonde and between the different retrievals. They are most pronounced in the boundary layer, where they can reach 24%. However, these values are very small if compared to the huge variability of tropospheric water vapour and we can use the H_2O profiles retrieved from the different spectral regions interchangeably.

In the 1090–1330 and 2650–3180 cm^{-1} regions we can detect δD profiles and distinguish between the lower and middle/upper tropospheric δD. The FTIR data are in good agreement with climatological data obtained from a variety of in-situ measurements. Furthermore, for both retrievals we observe very similar atmospheric δD variations and we can conclude that the retrievals produce lower and middle/upper tropospheric δD with a precision of better than 8 and 17‰, respectively. This is very satisfactory and affirms the large potential of the NDACC FTIR measurements in the field of water cycle research and satellite validation. Nevertheless, it is unsatisfactory that the systematic difference between the two δD retrievals reaches 40‰ in the middle/upper troposphere. Further studies are required in order to better understand and correct this.

Acknowledgements. M. Schneider was supported by the Deutsche Forschungsgemeinschaft via the project RISOTO (Geschäftszeichen SCHN 1126/1-1 and 1-2) and since May 2010 he has enjoyed a Ramón y Cajal Grant from the Spanish Ministry of Science and Innovation. We are grateful to the Goddard Space Flight Center for providing the temperature and pressure profiles of the National Centers for Environmental Prediction via the automailer system. Part of this work was performed at the Jet Propulsion Laboratory, California Institute of Technology, under contract with NASA.

Edited by: H. Worden

References

Craig, H.: Isotopic variations in meteoric waters, Science, 133, 1702–1703, 1961.

D'Eu, J.-F., Lemoine, B., and Rohart, F.: Infrared HCN Lineshapes as a Test of Galatry and Speed-dependent Voigt Profiles, J. Molec. Spectrosc., 212, 96–110, 2002.

Ehhalt, D. H.: Vertical profiles of HTO, HDO, and H_2O in the Troposphere, Rep. NCAR-TN/STR-100, Natl. Cent. for Atmos. Res., Boulder, Colo., 1974.

Frankenberg, C., Yoshimura, K., Warneke, T., Aben, I., Butz, A., Deutscher, N., Griffith, D., Hase, F., Notholt, J., Schneider, M., Schrejver, H., and Röckmann, T.: Dynamic processes governing lower-tropospheric HDO/H_2O ratios as observed from space and ground, Science, 325, 1374–1377, doi:10.1126/science.1173791, 2009.

Hase, F., Blumenstock, T., and Paton-Walsh, C.: Analysis of the instrumental line shape of high-resolution Fourier transform IR spectrometers with gas cell measurements and new retrieval software, Appl. Opt., 38, 3417–3422, 1999.

Hase, F., Hannigan, J. W., Coffey, M. T., Goldman, A., Höpfner, M., Jones, N. B., Rinsland, C. P., and Wood, S. W.: Intercomparison of retrieval codes used for the analysis of high-resolution, ground-based FTIR measurements, J. Quant. Spectrosc. Ra., 87, 25–52, 2004.

Herbin, H., Hurtmans, D., Clerbaux, C., Clarisse, L., and Coheur, P.-F.: $H_2^{16}O$ and HDO measurements with IASI/MetOp, Atmos. Chem. Phys., 9, 9433–9447, doi:10.5194/acp-9-9433-2009, 2009.

Kurylo, M. J. and Zander, R.: The NDSC – Its status after 10 years of operation, Proceedings of XIX Quadrennial Ozone Symposium, Hokkaido University, Sapporo, Japan, 167–168, 2000.

Kuze A., H. Suto, M. Nakajima, and T. Hamazaki: Thermal and near infrared sensor for carbon observation Fourier-transform spectrometer on the Greenhouse Gases Observing Satellite for greenhouse gases monitoring, Appl. Optics, 48, 6716–6733, 2009.

Miloshevich, L. M., Paukkunen, H., Vömel, H., and Oltmans, S. J.: Development and validation of a time lag correction for Vaisala radiosonde humidity measurements, J. Atmos. Ocean. Tech., 21, 1305–1327, 2004.

Miloshevich, L. M., Vömel, H., Whiteman, D. W., and Leblanc, T.: Accuracy assessment and correction of Vaisala RS92 radiosonde water vapor measurements, J. Geophys. Res., 114, D11305, doi:10.1029/2008JD011565, 2009.

Nassar, R., Bernath, P. F., Boone, C. D., Gettelman, A., McLeod, S. D., and Rinsland, C. P.: Variability in HDO/H_2O abundance ratios in the tropical tropopause layer, J. Geophys. Res., 112, D21305, doi:10.1029/2007JD008417, 2007.

Pałm, M., Melsheimer, C., Noël, S., Heise, S., Notholt, J., Burrows, J., and Schrems, O.: Integrated water vapor above Ny Ålesund, Spitsbergen: a multi-sensor intercomparison, Atmos. Chem. Phys., 10, 1215–1226, doi:10.5194/acp-10-1215-2010, 2010.

Randall, D. A., Wood, R. A., Bony, S., Colman, R., Fichefet, T., Fyfe, J., Kattsov, V., Pitman, A., Shukla, J., Srinivasan, J., Stouffer, R. J., Sumi, A., and Taylor, K. E.: Climate Models and Their Evaluation, In: Climate Change 2007: The Physical Science Basis, Contribution of Working Group I to the Fourth Assessment Report of the Intergovernmental Panel on Climate Change, edited by: Solomon, S., Qin, D., Manning, M., Chen, Z., Marquis, M., Averyt, K. B., Tignor, M., and Miller, H. L., Cambridge University Press, Cambridge, United Kingdom and New York, NY, USA, 2007.

Risi, C., Bony, S., and Vimeux, F.: Influence of convective processes on the isotopic composition (O^{18} and D) of precipitation and water vapor in the Tropics: Part 2: Physical interpretation of the amount effect, J. Geophys. Res., 113, D19306, doi:10.1029/2008JD009943, 2008.

Rodgers, C. D.: Inverse Methods for Atmospheric Sounding: Theory and Praxis, World Scientific Publishing Co., Singapore, ISBN 981-02-2740-X, 2000.

Rodgers, C. D. and Connor, B. J.: Intercomparison of remote sounding instruments, J. Geophys. Res., 108, 4116, doi:10.1029/2002JD002299, 2003.

Rothman, L. S., Gordon, I. E., Barbe, A., Chris Benner, D., Bernath, P. F., Birk, M., Boudon, V., Brown, L. R., Campargue, A., Champion, J.-P., Chance, K., Coudert, L. H., Dana, V., Devi, V. M., Fally, S., Flaud, J.-M., Gamache, R. R., Goldman, A., Jacquemart, D., Kleiner, I., Lacome, N., Lafferty, W. J., Mandin, J.-Y., Massie, S. T., Mikhailenko, S. N., Miller, C. E., Moazzen-Ahmadi, N., Naumenko, O. V., Nikitin, A. V., Orphal, J., Perevalov, V. I., Perrin, A., Predoi-Cross, A., Rinsland, C. P., Rotger, M., Simecková, M., Smith, M. A. H., Sung, K., Tashkun, S. A., Tennyson, J., Toth, R. A., Vandaele, A. C., and Vander-Auwera, J.: The HITRAN 2008 molecular spectroscopic database, J. Quant. Spectrosc. Radiat. Transfer, 110, 533–572, doi:10.1016/j.jqsrt.2009.02.013, 2009.

Schneider, M., Hase, F., and Blumenstock, T.: Water vapour profiles by ground-based FTIR spectroscopy: study for an optimised retrieval and its validation, Atmos. Chem. Phys., 6, 811–830, doi:10.5194/acp-6-811-2006, 2006a.

Schneider, M., Hase, F., and Blumenstock, T.: Ground-based remote sensing of HDO/H2O ratio profiles: introduction and validation of an innovative retrieval approach, Atmos. Chem. Phys., 6, 4705–4722, doi:10.5194/acp-6-4705-2006, 2006b.

Schneider, M. and Hase, F.: Technical Note: Recipe for monitoring of total ozone with a precision of around 1 DU applying mid-infrared solar absorption spectra, Atmos. Chem. Phys., 8, 63–71, doi:10.5194/acp-8-63-2008, 2008.

Schneider, M. and Hase, F.: Improving spectroscopic line parameters by means of atmospheric spectra: Theory and example for water vapour and solar absorption spectra, J. Quant. Spectrosc. Radiat. Transfer, 110, 1825–1839, doi:10.1016/j.jqsrt.2009.04.011, 2009a.

Schneider, M. and Hase, F.: Ground-based FTIR water vapour profile analyses, Atmos. Meas. Tech., 2, 609–619, doi:10.5194/amt-2-609-2009, 2009b.

Schneider, M., Romero, P. M., Hase, F., Blumenstock, T., Cuevas, E., and Ramos, R.: Continuous quality assessment of atmospheric water vapour measurement techniques: FTIR, Cimel, MFRSR, GPS, and Vaisala RS92, Atmos. Meas. Tech., 3, 323–338, doi:10.5194/amt-3-323-2010, 2010a.

Schneider, M., Yoshimura, K., Hase, F., and Blumenstock, T.: The ground-based FTIR network's potential for investigating the atmospheric water cycle, Atmos. Chem. Phys., 10, 3427–3442, doi:10.5194/acp-10-3427-2010, 2010b.

Schneider, M., Hase, F., Blavier, J.-F., Toon, G. C., and Leblanc, T.: An empirical study on the importance of a speed-dependent Voigt line shape model for tropospheric water vapor profile remote sensing, J. Quant. Spectrosc. Radiat. Transfer, in press, doi:10.1016/j.jqsrt.2010.09.008, 2010c.

Sussmann, R. and Borsdorff, T.: Technical Note: Interference errors in infrared remote sounding of the atmosphere, Atmos. Chem. Phys., 7, 353–3557, doi:10.5194/acp-7-3537-2007, 2007.

Sussmann, R., Borsdorff, T., Rettinger, M., Camy-Peyret, C., Demoulin, P., Duchatelet, P., Mahieu, E., and Servais, C.: Technical Note: Harmonized retrieval of column-integrated atmospheric water vapor from the FTIR network – first examples for long-term records and station trends, Atmos. Chem. Phys., 9, 8987–8999, doi:10.5194/acp-9-8987-2009, 2009.

Toon, G. C.: The JPL MkIV Interferometer, Opt. Photonics News, 2, 19–21, 1991.

Tran H., Bermejo, D., Domenech, J.-L., Joubert, P., Gamache, R. R., and Hartmann, J.-M.: Collisional parameters of H_2O lines: Velocity effects on the line shape, J. Quant. Spectrosc. Radiat. Transfer, 108, 126–145, 2007.

Wagner G. and Birk, M.: Water spectroscopy in the 1 µm region – a case study for collisional narrowing, 64th International Meeting on Molecular Spectroscopy, Columbus, Ohio, USA, June 22–26, 2009.

Worden, J. R., Bowman, K., Noone, D., Beer, R., Clough, S., Eldering, A., Fisher, B., Goldman, A., Gunson, M., Herman,

R., Kulawik, S. S., Lampel, M., Luo, M., Osterman, G., Rinsland, C., Rodgers, C., Sander, S., Shephard, M., and Worden, H.: TES observations of the tropospheric HDO/H2O ratio: retrieval approach and characterization, J. Geophys. Res., 111(D16), D16309, 10.1029/2005JD006606, 2006.

Worden, J. R., Noone, D., Bowman, K., Beer, R., Eldering, A., Fisher, B., Gunson, M., Goldman, A., Herman, R., Kulawik, S. S., Lampel, M., Osterman, G., Rinsland, C., Rodgers, C., Sander, S., Shephard, M., Webster, C. R., and Worden, H.: Importance of rain evaporation and continental convection in the tropical water cycle, Nature, 445, 528–532, doi:10.1038/nature05508, 2007.

Wunch, D., Toon, G. C., Blavier, J.-F., Washenfelder, R., Notholt, J., Connor, B. J., Griffith, D. W. T., Sherlock, V., and Wennberg, P. O.: The Total Carbon Column Observing Network (TCCON), Philos. T. R. Soc. A, accepted, 2010.

Yoshimura, K., Kanamitsu, M., Noone, D., and Oki, T.: Historical isotope simulation using Reanalysis atmospheric data, J. Geophys. Res., 113, D19108, doi:10.1029/2008JD010074, 2008.

Zahn, A.: Constraints on 2-Way Transport across the Arctic Tropopause Based on O_3, Stratospheric Tracer (SF_6) Ages, and Water Vapor Isotope (D, T) Tracers, J. Atmos. Chem. 39, 303–325, 2001.